Supplementary information:

Signal Amplification by Sensitive Control of Bifurcation Topology

R.B. Karabalin, Ron Lifshitz[2*], M.C. Cross[1], M.H. Matheny[1], S.C. Masmanidis[1], and M.L. Roukes[1†]

Kavli Nanoscience Institute and Condensed Matter Physics 114-36, California Institute of Technology, Pasadena, CA 91125, USA

[2] *Raymond and Beverly Sackler School of Physics & Astronomy, Tel Aviv University, Tel Aviv 69978, Israel*

*To whom correspondence on matters of theory should be addressed. E-mail: ronlif@tau.ac.il (RL).
[†]To whom correspondence on matters of experiment should be addressed. E-mail: roukes@caltech.edu (MLR).

Overview

In this document we present a theoretical exposition of how bifurcation topology can be controlled for a coupled pair of parametrically-driven nonlinear resonators. We then address the effect of noise on the probability that the system accurately follows the topology of the bifurcation. We subsequently provide further details about our experimental methods and on an apparatus for realizing a coupled-NEMS BTA. Finally, we assess the effective noise in our current implementation, and conclude by employing our noise analysis to make realistic projections of the ultimate sensitivity limits of this implementation.

* e-mail: roukes@caltech.edu

Theoretical Background

Response of Coupled Nonlinear Resonators to Parametric Excitation

We begin by providing the calculation of the theoretical response curves that are plotted in Fig. 1 of the main text. We consider two weakly-coupled parametrically-driven nonlinear resonators with slightly different normal frequencies. Their dynamics are governed by a pair of coupled equations of motion (EOM)

$$\frac{d^2\tilde{x}_\pm}{d\tilde{t}^2} + \tilde{\gamma}\frac{d\tilde{x}_\pm}{d\tilde{t}} + \left(\omega_\pm{}^2 + \tilde{h}\cos\tilde{\omega}_p\tilde{t}\right)\tilde{x}_\pm + \alpha\,\tilde{x}_\pm{}^3 + \tilde{\eta}\tilde{x}_\pm{}^2\frac{d\tilde{x}_\pm}{d\tilde{t}} + \tilde{D}(\tilde{x}_\pm - \tilde{x}_\mp) = 0, \qquad (S1)$$

where all physical parameters—after having divided out the effective mass of the resonators—are denoted with tildes to distinguish them from the scaled parameters used below. Here $\tilde{x}_+$ denotes the displacement of the higher-frequency resonator with frequency ω_+ from its equilibrium, and $\tilde{x}_-$ denotes the displacement from equilibrium of the lower-frequency resonator with frequency ω_-. The Duffing parameter α, the linear damping rate $\tilde{\gamma}$, and the coefficient of nonlinear damping $\tilde{\eta}$ are all assumed to be approximately the same for both resonators, and the coupling strength between the resonators is denoted by $\tilde{D}$. The parameters $\tilde{h}$ and $\tilde{\omega}_p$ are the parametric driving amplitude and driving frequency.

We rescale the units of time and space, to eliminate two additional parameters from the equation of motion—the average resonance frequency of the resonators, and the Duffing parameter, which are both set to 1. Because we drive the system close to twice the average resonance frequency, we express the scaled pump frequency as $\omega_p = 2 + \Delta\omega_p$. The EOM then becomes

$$\ddot{x}_{\pm} + Q^{-1}\dot{x}_{\pm} + \left(1 \pm \Delta + H\cos\left[2 + \Delta\omega_p\right]t\right)x_{\pm} + x_{\pm}^{3} + \eta x_{\pm}^{2}\dot{x}_{\pm} + D\left(x_{\pm} - x_{\mp}\right) = 0, \tag{S2}$$

where dots denote derivatives with respect to the dimensionless time t, Q is the quality factor of the resonators, and $\Delta \ll 1$ is the scaled frequency difference between the resonators, so that $\omega_{\pm}^{2}$ are replaced by $1 \pm \Delta$.

We calculate the response of the coupled resonators following the methods of Lifshitz & Cross (*1,2*). We begin by assuming that the linear damping is weak or, equivalently, that Q is large, and define a small expansion parameter ε, by expressing the scaled linear damping rate as $Q^{-1} = \varepsilon\gamma$, with γ of order unity. The parametric instability of the system then occurs for small driving amplitudes on the order of ε near resonance. If, in addition, we consider the system near the onset of the instability, we can assume that the effects of nonlinearity are small as well. Since the coupling strength is the weak signal to be amplified by the BTA, it can also be considered as a small perturbative correction. Finally, the frequency difference between the two resonators can also be taken to be small, on the order of ε. All these perturbative corrections can be chosen to enter the EOM in the same order of the small parameter ε by taking the leading order in $x_{\pm}$ to be $\sqrt{\varepsilon}$, expressing the scaled parametric driving amplitude as $H = \varepsilon h$, expressing the scaled frequency difference as $\Delta = \varepsilon\delta$, expressing the scaled coupling constant as $D = \varepsilon d$, and driving the system close to twice the average resonance, taking $\Delta\omega_p = \varepsilon\Omega$. The final form of the EOM is then

$$\ddot{x}_{\pm} + \varepsilon\gamma\dot{x}_{\pm} + \left(1 \pm \varepsilon\delta + \varepsilon h\cos[2 + \varepsilon\Omega]t\right)x_{\pm} + x_{\pm}^{3} + \eta x_{\pm}^{2}\dot{x}_{\pm} + \varepsilon d\left(x_{\pm} - x_{\mp}\right) = 0. \tag{S3}$$

Expecting the motion of the resonators away from equilibrium to be on the order of $\sqrt{\varepsilon}$ we try a solution of the form

$$x_{\pm}(t) = \frac{\sqrt{\varepsilon}}{2}\left(A_{\pm}(T)e^{it} + c.c.\right) + \varepsilon^{3/2}x_{\pm}^{(1)}(t) + \dots . \tag{S4}$$

The lowest order contribution to this solution is based on the solution to the linear equations of motion of the two simple harmonic oscillators $\ddot{x}_{\pm} + x_{\pm} = 0$, where $T = \varepsilon t$ is a slow time variable, allowing the complex amplitudes $A_{\pm}(T)$ to vary slowly in time, due to the effect of all the perturbative terms in Eq. (S3). Following the methods of Lifshitz & Cross[1,2] we obtain a pair of coupled equations for determining the amplitudes $A_{\pm}(T)$,

$$2i\frac{dA_{\pm}}{dT} + d\left(A_{\pm} - A_{\mp}\right) \pm \delta A_{\pm} + \frac{h}{2}A_{\pm}^{*}e^{i\Omega T} + i\gamma A_{\pm} + \frac{3+i\eta}{4}\left|A_{\pm}\right|^{2}A_{\pm} = 0 . \tag{S5}$$

The explicit time dependence can be removed by taking a solution of the form

$$A_{\pm}(T) = a_{\pm}(T)e^{i\frac{\Omega}{2}T} , \tag{S6}$$

yielding a corresponding equation for $a_{\pm}(T)$,

$$\left(2i\frac{d}{dT} + d \pm \delta - \Omega + i\gamma\right)a_{\pm} - da_{\mp} + \left(\frac{3+i\eta}{4}\right)\left|a_{\pm}\right|^{2}a_{\pm} = -\frac{h}{2}a_{\pm}^{*} . \tag{S7}$$

With the expression (S6) for the slowly varying amplitudes $A_{\pm}(T)$, the steady-state solution to the scaled equations of motion (S2), for which the complex amplitudes $a_{\pm}$ are constant in time, becomes an oscillation at half the drive frequency $1 + \varepsilon\Omega/2$. Note that we are not interested in

the corrections $x_{\pm}^{(1)}(t)$ of order $\varepsilon^{3/2}$ to these oscillations, but rather in finding the fixed complex amplitudes $a_{\pm}$ of the lowest order terms. These are obtained by solving the coupled algebraic equations, obtained from (S7) by requiring that $da_{\pm}/dT = 0$. Setting $d = 0$ decouples the equations, giving two equations that can be solved in closed from (*1,2*). The solution to a single equation gives the response curve, shown in Fig. 1a in the main text. The sum of both solutions, taking into account the relative π phase freedom, is plotted in Fig. 1b. For finite coupling $d \neq 0$ we can find the roots of the coupled Eqs. (S7) numerically once values are chosen for the different parameters. These are shown in Figs. 1c and 1d for positive and negative coupling respectively. In all plots we use the values $\gamma = 1$, $\eta = 0.01$, $\delta = 1.1$, and $h = 1.05$. In 1b we take $d = 0$, and in 1c and 1d we take $d = \pm 0.01$.

Amplitude Equation for an Imperfect Pitchfork Bifurcation

We wish to consider in more detail what happens at the bifurcation upon an upward frequency sweep, as the second mode starts oscillating. In the presence of weak coupling the normal modes are slightly modified from pure motion of the individual resonators. Diagonalization of the linear terms in (S7), keeping only corrections of order d/δ, yields the modified modes

$$\mathbf{v}^{(1)} = \begin{pmatrix} \dfrac{d}{2\delta} \\ 1 \end{pmatrix}, \quad \mathbf{v}^{(2)} = \begin{pmatrix} 1 \\ -\dfrac{d}{2\delta} \end{pmatrix}, \quad \text{with} \quad \begin{pmatrix} a_+ \\ a_- \end{pmatrix} = \sum_{n=1}^{2} a_n(T)\mathbf{v}^{(n)}, \tag{S8}$$

where the mode frequencies are unchanged to first order in d/δ. Substitution into Eq. (S7) yields a set of nonlinearly-coupled equations of motion for the modified mode amplitudes $a_n(T)$,

$$\left(2i\frac{d}{dT}-2\delta-\Omega_2+i\gamma\right)a_1+\left(\frac{3+i\eta}{4}\right)\left[|a_1|^2a_1+\frac{d}{\delta}\left(\frac{1}{2}|a_2|^2a_2-|a_1|^2a_2-\frac{1}{2}a_1^2a_2^*\right)\right]=-\frac{h}{2}a_1^*, \quad (S9)$$

$$\left(2i\frac{d}{dT}-\Omega_2+i\gamma\right)a_2+\left(\frac{3+i\eta}{4}\right)\left[|a_2|^2a_2+\frac{d}{\delta}\left(-\frac{1}{2}|a_1|^2a_1+|a_2|^2a_1+\frac{1}{2}a_2^2a_1^*\right)\right]=-\frac{h}{2}a_2^*, \quad (S10)$$

where we now measure the drive frequency with respect to the second mode frequency by defining $\Omega_2=\Omega-(d+\delta)$.

Our aim is to obtain an equation for the growth of the amplitude of the second mode at the bifurcation, as the frequency is swept upward. At that point the first mode will have already reached a certain non-zero amplitude, which can be determined analytically (*2*) by solving (S9) after setting $a_2=0$. To find the initial growth of the second mode we linearize (S10) in a_2. Taking the coupling d/δ to be weak, and assuming an initial growth of the form

$$a_2=ae^{i\left(\frac{\pi}{4}+\phi\right)}e^{\sigma T}, \quad \text{with} \quad a,\phi,\sigma\in\Re, \quad (S11)$$

we find that the phase ϕ and the growth rate σ satisfy the relations

$$2\sigma=-\gamma+\frac{h}{2}\cos 2\phi,$$
$$0=\Omega_2+\frac{h}{2}\sin 2\phi. \quad (S12)$$

Thus, the bifurcation occurs as the drive frequency Ω_2 is increased and reaches a critical value of $\Omega_C=-\sqrt{(h/2)^2-\gamma^2}$.

Next, we wish to include nonlinearity to saturate the growth of the second mode, and to include the coupling to the first mode, which is already oscillating, to affect the topology of the bifurcation. Performing a calculation similar to that found in section 1.3.3 of Lifshitz & Cross (*2*), we find that

$$a_2 = B(T)e^{i\left(\frac{\pi}{4}+\phi\right)},$$ (S13)

where the real-valued saturated amplitude $B(T)$ satisfies the equation

$$\frac{dB}{dT} = (\Omega_2 - \Omega_C)\frac{|\Omega_C|}{2\gamma}B - \frac{1}{8}\left(\frac{3|\Omega_C|}{\gamma}+\eta\right)B^3 + \frac{d}{\delta}\frac{h\sqrt{9+\eta^2}}{32\gamma}|a_1|^3\sin\left(\phi+\hat{\phi}_1-\frac{\pi}{4}\right),$$ (S14)

where $|a_1|$ is the amplitude of the first mode determined earlier, and $\hat{\phi}_1$ is the phase ϕ_1 of the first mode plus $\arctan(\eta/3)$. It can be shown that for weak nonlinear damping $(\eta << 1)$, $\hat{\phi}_1 \cong \phi + \pi/4$.

Scaling back to the parameters of Eq. (S2), and dropping terms of order η^2 we find that at the bifurcation the modes [with eigenvectors given by (S8)] are oscillating as

$$x_1(t) = X_1\cos\left(\left[1+\frac{\Delta\omega_p}{2}\right]t+\phi_1\right),$$

$$x_2(t) = X_2(t)\cos\left(\left[1+\frac{\Delta\omega_p}{2}\right]t+\frac{\pi}{4}+\phi\right).$$ (S15)

The amplitude of the second mode $X_2(t)$ satisfies the equation

$$\frac{dX_2}{dt} = \left(\Delta\omega_p - \left[D + \Delta - \omega_C\right]\right)\frac{Q\omega_C}{2} X_2 - \frac{1}{8}\left(3Q\omega_C + \eta\right)X_2^{\ 3} + \frac{3}{16}\frac{D}{\Delta}Q\omega_C X_1^{\ 3}, \tag{S16}$$

which has the typical form of an imperfect pitchfork bifurcation, with $\Delta\omega_p$ acting as the control

parameter, and where $Q\omega_C = \sqrt{\left(\frac{QH}{2}\right)^2 - 1}$.

Analysis of the Effects of Noise

Noise in the system will have its largest effect on the measurement process as the pump

frequency passes through the pitchfork bifurcation of the second mode. The dynamics in this

vicinity can be analyzed using Eq. (S16) for the amplitude of the second mode, supplemented

with a noise term. For small signal and noise the important time range is when X_2 is small, so

that the nonlinear term in Eq. (S16) is not involved. We write the linearized Eq. (S16) in the

form

$$\frac{dX_2}{dt} = rtX_2 + s + f(t) \tag{S17}$$

where rt is the linear ramp of control parameter (the parameters in front of X_2 in the first term on

the right hand side of Eq. (S16)) choosing to measure time t from the bifurcation point, s is the

term leading to the imperfect bifurcation proportional to the coupling D (the last term in Eq.

(S16)), and $f(t)$ is the noise force term, assumed to be Gaussian white noise of strength F defined

by

$$\langle f(t)f(t')\rangle = 2F\delta(t - t'). \tag{S18}$$

The conventional force spectral density S_F is related to this noise strength by $S_F = 4F$. The Fokker-Planck equation for the probability distribution $P(X_2)$ of X_2 at time t corresponding to Eq. (S17) can be solved to give the Gaussian distribution

$$P(X_2) = \frac{1}{\sqrt{2\pi}\sigma(t)} e^{-[X_2 - X_D(t)]^2 / 2\sigma^2(t)}, \tag{S19}$$

where $X_D(t)$ is the deterministic solution, given by equation (S17) without the noise term, and $\sigma(t)$ is the time dependent width. $X_D(t)$ grows away from zero due to the signal s. The explicit expressions, assuming the control parameter ramp starts at a value far below the bifurcation point, are

$$X_D(t) = s \int_{-\infty}^{t} e^{r(t^2 - t'^2)/2} dt',$$
$$\sigma^2(t) = 2F \int_{-\infty}^{t} e^{r(t^2 - t'^2)} dt'. \tag{S20}$$

For long times $t \gg r^{-1/2}$ these expressions give

$$X_D(t) = \left(\frac{2\pi}{r}\right)^{1/2} s\, e^{rt^2/2},$$
$$\sigma(t) = \left(\frac{4\pi}{r}\right)^{1/4} F^{1/2} e^{rt^2/2}. \tag{S21}$$

Note the super-exponential growth of both the center and width of the distribution due to the increasing amplification rate, proportional to the bifurcation parameter rt. We now calculate the probability $P_\uparrow$ that at long times X_2 falls in the basin of attraction of the $\uparrow$ branch (and $P_\downarrow = 1 - P_\uparrow$). The shift $-s/rt$ in the basin boundary away from $X_2=0$ is small compared with X_D

for $t \gg r^{-1/2}$, and so $P_\uparrow \approx \int_0^\infty P(X_2) dX_2$ giving

$$P_\uparrow - P_\downarrow \approx \mathrm{erf}\left(\frac{X_D}{\sqrt{2}\sigma}\right) = \mathrm{erf}\left[\left(\frac{\pi}{4}\right)^{1/4} \frac{s}{r^{1/4} F^{1/2}}\right]. \tag{S22}$$

Note that the expression for $P_\uparrow - P_\downarrow$ is independent of time, and we may choose any time for its evaluation that is long enough compared with $r^{-1/2}$ so that the approximations we have made are good, but short enough so that the nonlinear term in the evolution equation is not yet important. Such a time always exists for the limit of small signal and noise of interest. Also note that the effective bandwidth for the noise appearing in the "signal to noise" ratio in the argument to the error function in Eq. (S22) is $r^{1/2}$ and is determined by the frequency ramp-rate.

As we show below in Eq. (S27), the BTA output signal is proportional to $P_\uparrow - P_\downarrow$. For the limit of small signals Eq. (S22) reduces to

$$P_\uparrow - P_\downarrow \approx \left(\frac{4}{\pi}\right)^{1/4} \frac{s}{r^{1/4} F^{1/2}} . \tag{S23}$$

For M sweeps through the bifurcation, the distribution of the fraction of up traces follows Poisson statistics, which for large M reduces to a Gaussian with mean $P_\uparrow$, and standard deviation $1/\sqrt{2M}$ for $P_\uparrow$ close to 1/2. For a sweep rate $v_{sw} = \omega_{sw}/2\pi$, this leads to the error estimate for the measurement of the signal s of $\left(\sqrt{\pi r} S_F / 4 v_{sw}\right)^{1/2} / \sqrt{\text{Hz}}$.

The noise term $f(t)$ in Eq. (S17) ultimately derives from physical noise forces on the beams $\tilde{f}_\pm(\tilde{t})$ with $\left\langle \tilde{f}_\pm(\tilde{t}) \tilde{f}_\pm(\tilde{t}') \right\rangle = 2 \tilde{F} \delta_\pm \delta(\tilde{t} - \tilde{t}')$ leading to terms $\tilde{f}_\pm(\tilde{t})/m$ on the right hand side of Eq. (S1). Proceeding through the transformations as in Eqs. (S2)-(S16) leading to the evolution equation for X_2, but now including this noise term, relates the force strength in Eq. (S17) to these fundamental forces. For small beam coupling, the dominant noise source is just from the higher frequency beam, and then we find

$$F = \frac{1}{2} \frac{\alpha}{(m\omega_0^2)^3} \left(\frac{QH}{2}\right)^2 \tilde{F} . \tag{S24}$$

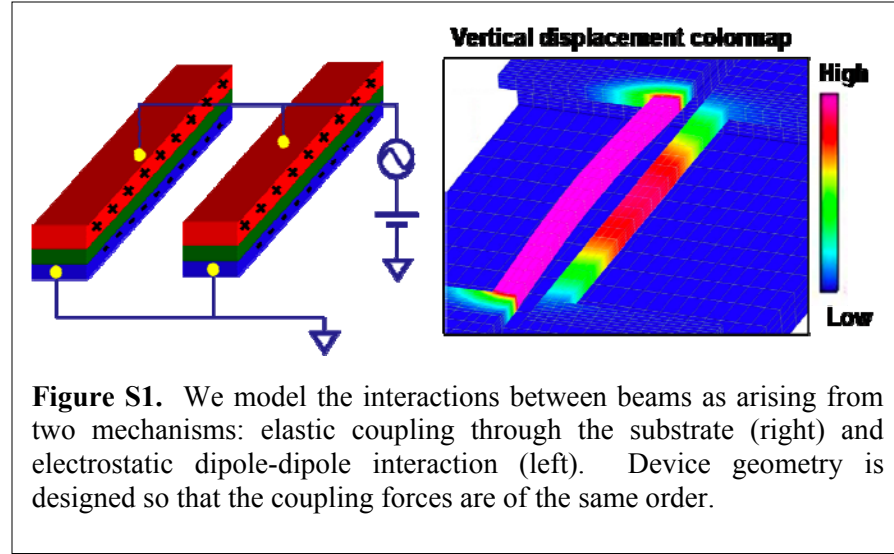# Fabrication and Methods

Device Fabrication: Coupled-NEMS BTA

Fabrication is based on a GaAs-based multilayer grown by molecular beam epitaxy (MBE) upon a GaAs substrate. The device structural layer itself is a 200nm thick multilayer structure, comprising a stack of three layers forming a vertically-oriented (*i.e.* out of the wafer plane) *p-i-n* diode: a topmost 100 nm *n*-GaAs (10^{19} cm^{-3}) layer, a 50 nm *i*-GaAs layer, and a 50 nm *p*-GaAs (10^{18} cm^{-3}). The *i*-GaAs layer has a *p*-type background concentration of ~5×10^{15}cm^{-3} arising from natural impurities, which is negligible compared to the intentionally doped regions. These structural *p-i-n* diode layers are grown on a sacrificial *p*-Al$_{0.8}$Ga$_{0.2}$As (10^{18} cm^{-3}) layer, which in turn is grown on a *p*-doped (10^{18} cm^{-3}) GaAs (001) substrate by MBE. The lead frame structure and wire bond pads are patterned by photolithography. This is followed by deposition of a thin ~5nm Ti adhesion layer and a 50nm Au layer, subsequently standard liftoff is employed. The backside of the p^{+}-doped wafer is coated with Ti/Au in order to provide a bottom electrical contact. The NEMS devices themselves are defined by electron beam lithography, which is followed by deposition of a 60nm Ti layer and liftoff. This Ti mask layer protects the desired structural regions during a dry etch using argon ion-beam milling to a depth of 250 nm. Subsequently, the patterned devices are suspended by removing the sacrificial Al$_{0.8}$Ga$_{0.2}$As layer using a selective, wet chemical etch in dilute hydrofluoric acid. This step also removes the Ti masks, exposing the Au electrodes and pads.

Coupling

Two different physical phenomena contribute to the coupling between beams: elastic mechanical coupling mediated through the substrate, and an electrostatic dipole-dipole interaction between

adjacent *p-i-n* diode structures in the voltage-biased beams. We discuss each mechanism in turn; they are pictorially depicted in Figure S1.

Figure S1. We model the interactions between beams as arising from two mechanisms: elastic coupling through the substrate (right) and electrostatic dipole-dipole interaction (left). Device geometry is designed so that the coupling forces are of the same order.

Electrostatic Coupling. When a DC bias voltage is applied to both beams, charges of opposite sign accumulate on their top and bottom surfaces forming dipole moments. Two such identical dipoles interact electrostatically with a force (*3*)

$$F_{dipoles} = -\frac{9}{4\pi\varepsilon_0}\frac{(\varepsilon_0\varepsilon A_{beam})^2}{d^5}\left(V_{bias} + \psi_0\frac{t_m}{t_i}\right)^2 (x_1 - x_2), \tag{S25}$$

where d is the distance between the beams, A_{beam} is a beam's surface area $L \times w$, x_1 and x_2 are the out-of-plane displacements at the center of the beams, $\psi_0 \approx 1.2$V is a built-in potential, $t_i = 50$nm is the thickness of the insulating layer, and $t_m \approx 78$nm is the depletion width of the *p-i-n* diode (*4*).

This coupling has a simple linear form with a negative coefficient, meaning a repulsive interaction ensues. This arises from the fact that, with the same voltage applied to both beams, dipole moments of the same orientation develop in the beams. For the geometry of the devices used in these experiments ($d=400$nm, $A_{beam} = L \times w = 6\mu$m$\times0.5\mu$m, and $V_{offset} \approx 1.1$V), a force of approximately -1pN is generated from a 1nm difference in displacements.

Mechanical Coupling. Without any applied voltage there is residual attraction between the beams due to elastic coupling through their shared elastic support, even though no ledge is shared by the beams. Finite element numerical simulations are used to estimate the magnitude of elastic coupling mediated through the substrate, the displacement colormap of the mechanically interacting beams is shown in Figure S1. We find the interaction to be attractive and linearly dependent on displacement difference. We design the geometry of the system so that at the difference in displacements of ~1nm, the effective mechanical coupling force is approximately ~1pN, as a result the dipole–dipole interaction compensates the elastic coupling within experimentally accessible voltage range.

Summary of Measurement Apparatus and Methods

Samples are mounted in a room temperature vacuum chamber, which is pumped down to a typical pressure of 5 mTorr for experiments. This chamber is fitted with a transparent sapphire optical window to enable optical interferometry, however to minimize the impact of spurious light on device performance (for example, due to heating and inadvertent generation of photocarriers) we place a neutral density filter with a 10-fold extinction factor in front of the optical port. Illumination is provided by an infrared laser diode emitting 2 mW at 904 nm. The laser is focused to a spot of ~10 μm in diameter upon the device. The reflected signal is detected by a low-noise, high-bandwidth photoreceiver (New Focus 1801, bandwidth=125 MHz, optical noise power spectral density = 30 pW/√Hz, referred to input).

We calibrate the displacement response of the interferometer using the known amplitude at the onset of nonlinear response for doubly-clamped beams, which arises from the Duffing instability. Direct frequency response measurements for the coupled resonators are made using an RF vector network analyzer (Hewlett Packard 3577A) as shown in Figure S2. The amplitudes of the two peaks are different
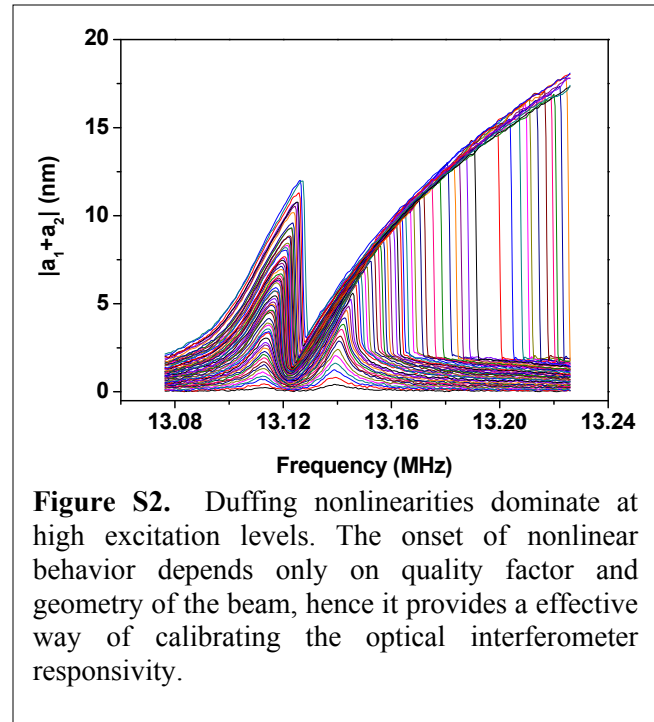

Figure S2. Duffing nonlinearities dominate at high excitation levels. The onset of nonlinear behavior depends only on quality factor and geometry of the beam, hence it provides a effective way of calibrating the optical interferometer responsivity.

due to slight variations in their actuation efficiencies. The family of curves displayed represents drive amplitudes from 50mV$_{rms}$ to 1.2V$_{rms}$. The onset of nonlinearity occurs for a ~600mV$_{rms}$ drive level, which yields an optical signal of approximately 70μV$_{rms}$. The estimated accuracy of this calibration is of order 10%.

We have configured the sample geometry and experimental apparatus so that the laser spot illuminates both NEMS resonators simultaneously. In this case the output from the photodetector represents the summed contribution from the coupled beams. As described in the main text, the response to a parametric pump signal in the 26MHz range is for both beams to become excited when the pump is roughly twice their natural resonance frequency. Depending on the sign of $V_{in}(t)$ the pump induces coupled vibrations that are either in-phase (yielding strong optical reflection) or out-of-phase (giving a weak optical response). Parametric frequency sweeps are measured with a spectrum analyzer (Agilent 4395A).
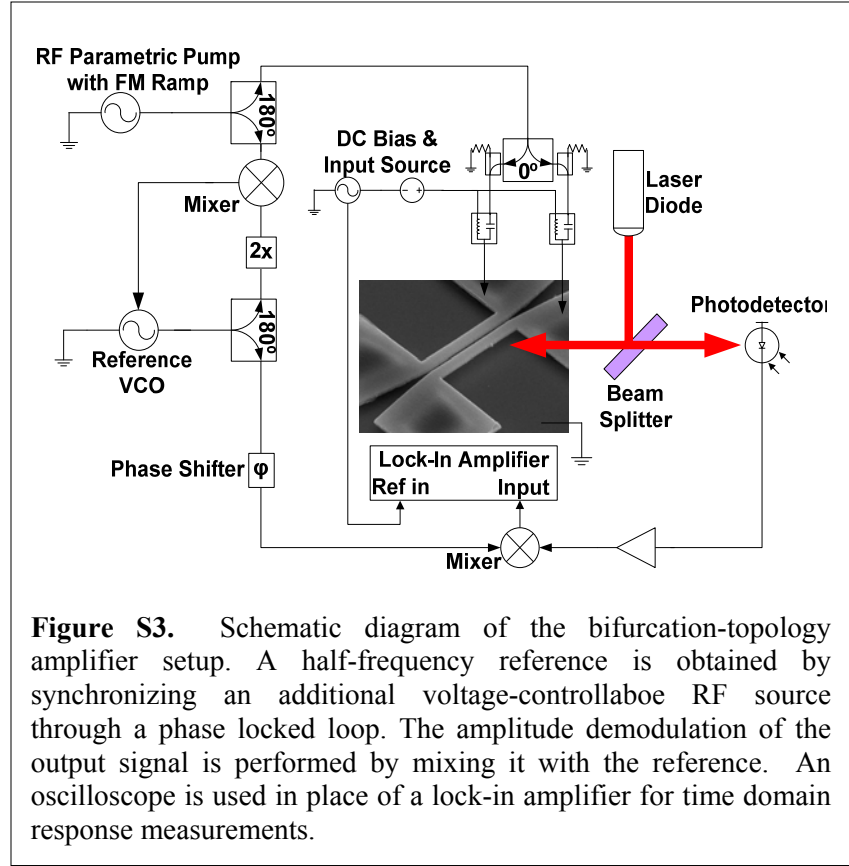
BTA Measurement Protocol

To evaluate the BTA's performance we first null the beam-beam coupling with a DC input signal set to $V_{in}^{(DC)} = 0V$. Then, to simulate a small-signal input to be amplified, we add to this static input a simple single-tone, square-wave periodic waveform of the form $V_{in}^{(AC)}(t) = v_{in} \, sq(\omega_{in} t)$, where $sq(\omega_{in} t)$ is a square-wave function that changes from -1 to +1 with a period of $T_{in} = 1 / \omega_{in}$. We use typical input frequencies $\omega_{in} / (2\pi) \sim 170 Hz$. This can be increased without significant change to the output signal if ω_{in} remains a factor of 2 lower than the sweep rate discussed below. A function generator (Agilent 33250A) is used to source both the (summed) DC and AC input voltages simultaneously; this summed signal is applied to both NEMS actuation electrodes via a DC/RF bias tee.

The function generator (Agilent 33250A) used to provide the aforementioned ~26MHz parametric pump signal, provides is own internal frequency modulation in the form of a triangular sweep signal (ramp waveform) to provide an output with instantaneous frequency

$$\omega(t) = \omega_{bif} + \left[-\omega_{offset} + \Delta\omega_{sw} \, rmp(\omega_{sw} t) \right]. \tag{S26}$$

Here, $rmp(\omega_{sw} t)$ is a triangle function that changes from 0 to 1 and back again with period $T_{sw} = 1 / \omega_{sw}$. This frequency modulation serves to sweep the pump signal through the bifurcation point, ω_{bif}, starting from a frequency $\omega_{bif} - \omega_{offset}$ below it, to a frequency $\omega_{bif} + \left[\Delta\omega_{offset} - \Delta\omega_{sw} \right]$ above it. In most of our measurements an FM rate $\omega_{sw} / (2\pi) = 557 Hz$ is used. However, for our study of BTA amplification bandwidth, as described in the main text, this was varied between 70Hz and 3kHz. As mentioned, a 3dB decrease in gain was observed for $\omega_{sw} / (2\pi) \sim 2 kHz$.

A reference signal at half the pump frequency (~13MHz), in the range of the natural resonance frequencies of the NEMS is required to demodulate the photodetector output. This signal, of the form $V_{LO}\cos\left[\omega(t)t + \varphi_{LO}\right]$, is generated by phase locking a separate voltage-controlled oscillator to the pump, as shown in Figure S3. To lock

Figure S3. Schematic diagram of the bifurcation-topology amplifier setup. A half-frequency reference is obtained by synchronizing an additional voltage-controllaboe RF source through a phase locked loop. The amplitude demodulation of the output signal is performed by mixing it with the reference. An oscilloscope is used in place of a lock-in amplifier for time domain response measurements.

the pump and reference generators, an error signal is developed by homodyne converting the doubled reference output against the pump signal. The reference signal generated in this manner serves as the local oscillator for homodyne conversion of the photodetector's radio frequency output signal. The reference phase φ_{LO} is set by a phase shifter to maximize the mixer's phase-sensitive baseband output.

Consequently, the measured output of the BTA gives the r.m.s. summed displacements of the two resonators, which we express in nanometers. The summed displacement is averaged over the frequency sweep range, and over many sweeps, to give

$$V_{out} = P_{\uparrow}a_{\uparrow} + P_{\downarrow}a_{\downarrow} = \frac{a_{\uparrow} + a_{\downarrow}}{2} + \left(P_{\uparrow} - P_{\downarrow}\right)\frac{a_{\uparrow} - a_{\downarrow}}{2}, \tag{S27}$$

where $P_\uparrow$ ($P_\downarrow$) is the probability of following the upper (lower) branch, and $a_\uparrow$ ($a_\downarrow$) is the averaged summed displacement of the two resonators along the upper (lower) branch. Thus, to within a constant shift, the BTA output is proportional to the difference in probabilities $P_\uparrow - P_\downarrow$, and to the area that is confined between the two branches.

For time-domain measurements of the demodulated signal, a digital oscilloscope (Agilent 54622D) is employed, as shown in the inset of Fig. 3b in the main text. For frequency and amplitude sweeps to characterize BTA performance, the baseband signal is fed to a lock-in amplifier (Stanford Research System SR830), which is externally synched to $V_{in}(t)$.

Noise and Sensitivity Analysis

Noise and Sensitivity Analysis for the Current Implementation

In our experimental implementation of the BTA, the output signal is proportional to the difference in probabilities $P_\uparrow - P_\downarrow$ (S27). We fit the measured output signal to the predicted error function given by Eq. (S22). From the fit, shown in Fig. 4(c) of the main text, using the known parameters of the beam, we extract the effective force noise strength $S_F^{1/2}$ acting on the beam. We find an effective force noise of $1.8 \times 10^{-13} N/\sqrt{Hz}$ in our experimental setup, which corresponds to effective charge sensitivity of 39 e/√Hz.

Alternatively we can determine the sensitivity of our measurement setup by direct noise measurements. The inset of Fig. 4a displays the smallest input signal characterized in this study, $V_{in}^{(AC)} = 1$ mV. This corresponds to about 70e (e=1.6×10^{-19} C) in the conducting layers of the *p-i-n* stack in each resonator. A Gaussian fit shows that the magnitude of the induced displacement response is ~1.22 nm. From this we obtain a displacement-to-charge responsivity for the BTA of $\partial x/\partial q \sim 17$ pm/e. For the measurement bandwidth Δf employed (see below), intrinsic noise measurements with no input signal yield a displacement noise in the output signal of $(S_x \Delta f)^{1/2} \sim 126\text{pm}$, which is consistent with the Poisson statistics of equal probabilities of following the up and down branches. This corresponds to an electronic charge noise of $(S_q \Delta f)^{1/2} = (S_x \Delta f)^{1/2}(\partial q/\partial x) \sim 7.3\text{e}$.   For these measurements a four-pole Butterworth filter (roll off = 24dB/octave) with a time constant of τ=0.3s was employed. The resulting sweep was averaged *N*=22 times, thus yielding an equivalent noise bandwidth $\Delta f = 5/(64\tau\sqrt{N}) \sim$ 0.056 Hz. Accordingly, the demonstrated charge sensitivity is $S_q^{1/2} \sim 31$ e/√Hz. This result is consistent with our previous estimate obtained by fitting the amplifier transfer function to an error function.

In our present implementation, the noise in the system is primarily limited by non-idealities in the measurement system; we believe significant further optimization is possible.

Principal Fundamental Noise Mechanisms of a Coupled-NEMS BTA

Assuming the displacement sensitivity of the measurement setup is improved to the extent that the thermomechanical noise of both resonator can be measured we then analyze the limits of the sensitivity of coupled-NEMS BTA. Among the fundamental noise sources are:

I. Thermomechanical motion of the NEMS resonators. The thermomechanical noise force is caused by the Brownian motion of the NEMS resonator. Near the bifurcation point one resonator is excited while the other is still dormant, and so the contribution of the thermomechanical motion of the first resonator is negligible. The noise floor of the second resonator is set by the thermomechanical force noise power spectral density, $S_{F,th}^{1/2} = \sqrt{4k_B T m \omega_+ / Q}$, where k_B is a Boltzman constant, T is room temperature, and m is the effective mass of the resonator. For our beam dimensions this value is $S_{F,th}^{1/2} = 1.6 \times 10^{-15} N / \sqrt{Hz}$.

II. Thermal charge fluctuations on the beam electrodes. These serve to induce a fluctuating force on the BTA which can drive transitions at the bifurcation point. Their magnitude can be estimated using the equipartition theorem for the charge noise in the beam electrode, $<q^2>/C = k_B T$. This energy is distributed over the RC bandwidth, with R the load resistance and C the interlayer electrode capacitance. By separating the measurement electrodes from the drive electrodes (not done in the present implementation), and by tuning the external load resistance, the charge fluctuation noise can be confined to a narrow region

outside the measurement bandwidth, so that this noise source becomes negligible in the measurements.

III. <u>Noise in the beam coupling</u>. To estimate this contribution we calculate the electrostatic interaction force to next order in the relative displacement, $O(x_1 - x_2)^3$. This is given by $F_{dipole} \sim \Delta_1(x_1 - x_2) + \Delta_3(x_1 - x_2)^3$, where we find from an analysis of the electrostatics $\Delta_3 = 75\Delta_1 / (2d^2)$. Therefore the equivalent force noise spectral density is $S_{F_{dipole}}^{1/2} = \Delta_3 \langle x_1 \rangle S_{x_1}^{1/2} \langle x_2 \rangle$, where $\langle x_1 \rangle$ and $\langle x_2 \rangle$ are the r.m.s. displacements of the first and second resonators respectively, and $S_{x_1}^{1/2}$ is the spectral density of the thermomechanical displacement thermal noise of the first resonator. For the system of coupled beams employed in our BTA implementation the coupling force noise is $S_{F,dipole}^{1/2} = 8.2 \times 10^{-18} N / \sqrt{Hz}$, which is 200 times smaller than the thermomechanical noise calculated in I, above.

Projections of the Ultimate Sensitivity of a Coupled-NEMS BTA

The dominant thermomechanical noise source, calculated in I of the previous section, is used to estimate the fundamental limits to the charge sensitivity of our first implementation of the coupled-NEMS BTA that are quoted in the main text. For our present device we estimate that a thermodynamically limited sensitivity of 0.46e/√Hz should be achievable at room temperature. For a 1GHz device (*6*), with reduced capacitance due to its smaller geometry, operating at 300mK as a base temperature (*7*), we estimate that a sensitivity of order 1×10^{-5} e/√Hz is feasible. In order for such device to be implemented at cryogenic temperatures the phase sensitive transduction scheme needs to be realized. At room temperature we used optical interferometry

which is capable of distinguishing in and out of phase motion. On the one hand optical detection techniques proved to be compatible with cryogenic measurements(8). Alternatively there are wide variety of all-electric transduction techniques ranging from electrostatic, to piezoelectric, to magnetomotive that are phase sensitive, so that BTA architecture can be implemented.

References

1. R. Lifshitz, M. C. Cross, Response of parametrically driven nonlinear coupled oscillators with application to micromechanical and nanomechanical resonator arrays. *Physical Review* B **67**, 134302 (2003).

2. R. Lifshitz, M. C. Cross, Nonlinear dynamics of nanomechanical and micromechanical resonators. in *Annual Review of Nonlinear Dynamics and Complexity*. Edited by H.G. Schuster (Wiley, New York, 2008) pp. 1–52.

3. H. X. Tang, X. M. H. Huang, M. L. Roukes, M. Bichler, W. Wegscheider, Two-dimensional electron-gas actuation and transduction for GaAs nanoelectromechanical systems. *Applied Physics Letters* **81**, 3879-3881 (2002).

4. S. C. Masmanidis *et al.*, Multifunctional nanomechanical systems via tunably-coupled piezoelectric actuation. *Science* **317**, 780 (2007).

5. A. N. Cleland, M. L. Roukes, Noise processes in nanomechanical resonators. *Journal of Applied Physics* **92**, 2758–2769 (2002).

6. X. M. H. Huang, C. A. Zorman, M. Mehregany, M. L. Roukes, Nanodevice motion at microwave frequencies. *Nature* **421**, 496 (2003).

7. A. Naik *et al*. Cooling a nanomechanical resonator with quantum back-action. *Nature* **443**, 193–196 (2006).

8. D. Rugar, R. Budakian, H. J. Mamin, B. W. Chui, Single spin detection by magnetic resonance force microscopy. *Nature* **430**, 329(2004)